PCCP

ROYAL SOCIETY OF CHEMISTRY

PAPER

View Article Online
View Journal | View Issue

Cite this: *Phys. Chem. Chem. Phys.*, 2026, **28**, 6786

Electronic properties and electrical mobilities of cationic silver hydride clusters

Somnath Bhowmick, *[a] Mohsen Doust Mohammadi, [a] Anne Maisser [a] and George Biskos *[ab]

Cationic silver hydride clusters (Ag_nH^+) can be formed by a number of physical and chemical processes, holding great promise for a range of applications including photonics, catalysis, sensing, and biomedicine, among others. Here, we present a comprehensive theoretical investigation of Ag_nH^+ clusters (n = 1–7) using highly accurate coupled-cluster (CC) theory. Multiple low-lying isomers are identified using CC theory with single and double excitations (CCSD), whereas their relative stabilities are determined with the more accurate CCSD(T) method. The CCSD(T) results predict a pronounced odd–even alternation in relative stabilities, with Ag_2H^+ being the most stable species, which is consistent with experimental mass spectrometry measurements. *Ab initio* molecular dynamics simulations show that all low-energy isomers remain structurally rigid at room temperature, whereas bonding analyses (frontier molecular orbitals, natural bond orbital, molecular electrostatic potential, quantum theory of atoms in molecules, non-covalent interaction) indicate strong ionic Ag–H interactions, weak non-covalent Ag–Ag interactions, and significant donor–acceptor stabilization in larger clusters. Electrical mobilities of these clusters, computed by the trajectory method, were labelled on experimental spectra, in order to contribute towards their interpretation. Overall, our results resolve inconsistencies from prior theoretical predictions, provide a rigorous description of cationic silver hydride clusters, and are used to improve the interpretation of earlier observations.

Received 16th December 2025,
Accepted 16th February 2026

DOI: 10.1039/d5cp04890g

rsc.li/pccp

1 Introduction

Silver (Ag) has long been valued for its unique properties that enable applications ranging from uses in ancient medicinal practices[1,2] to modern nanotechnology.[3] Ag-based atomic clusters expand the potential of this material for applications in catalysis,[4] sensing,[5] optoelectronics,[6] plasmonics,[7] biomedicine,[8] and DNA sequencing,[9] among others, due to their unique physico-chemical properties that differ considerably from those of nanoparticle and bulk material counterparts,[10,11] and are strongly size-dependent.[12–15]

Earlier experimental investigations show that ionic silver clusters readily undergo reactions with oxygen and water, leading to the formation of oxidized products.[16–24] The stability of these oxidized species is strongly influenced by the size and electronic configurations, *i.e.*, open or closed-shell, of the clusters.[18,19,22] Beyond that, ionic Ag clusters have also been shown to react with a range of other small gas-phase molecules, including N_2,[23] CO,[17,24] NO,[25,26] and halogenated compounds.[27,28] Their reactions with CO are strongly size-dependent, with even-numbered clusters showing enhanced activity towards CO oxidation compared to their odd-numbered counterparts. Similarly, reactions with NO reveal clear correlations between electronic configuration, *i.e.*, open and closed-shell, and reactivity.[25,26]

In our previous work, we studied a small range of cationic silver oxide clusters, specifically $Ag_nO_k^+$ with n = 1 to 4 and k = 1 to 5, using highly accurate *ab initio* methods to determine their ground-state geometries and relative stabilities.[29] The findings of that work show a clear trend: clusters with a single oxygen atom (k = 1) are more stable than those carrying more oxygen atoms, primarily due to the lack of weakly bound terminal O_2 units. Following that, we carried out additional calculations to determine the structures, stabilities, and chemical bonding of both cationic and anionic hydroxylated silver clusters ($AgO_kH_m^{\pm}$) with k and m = 1 to 4.[30] The results of our previous study also suggest that the ground states of many of these clusters are energetically stable, and that the presence of 3-center, 4-electron (3c/4e) "hyperbonds"[31] significantly contributes towards stability in many anionic clusters, as indicated by natural bond orbital[32] analysis.

Although traditional *ab initio* methods such as Hartree–Fock (HF) and density functional theory (DFT) have been widely used

[a] *Climate & Atmosphere Research Centre, The Cyprus Institute, 20 Konstantinou Kavafi Street, Nicosia 2121, Cyprus. E-mail: s.bhowmick@cyi.ac.cy, g.biskos@cyi.ac.cy; Fax: +357 22208625; Tel: +357 22 208618*
[b] *Faculty of Civil Engineering and Geosciences, Delft University of Technology, Delft, 2628 CN, The Netherlands*

to investigate both pure and heteroatomic silver cluster ions,[14,17,18,21,22,24,27,28,33–41] we recently demonstrated[29,30] that more accurate predictions of ground-state geometries and relative stabilities require robust electronic structure methods, such as the coupled-cluster theory with single, double, and perturbative triple excitations (CCSD(T)).[42–44] In fact, predictions of the ground-state structure of Ag_2O^+ vary markedly depending on the theoretical method employed.[17,22,38,39] HF calculations suggest a linear geometry,[17] whereas the DFT method predicts either linear[38] or bent[22,39] geometries depending on the exchange–correlation functional. CCSD(T) simulations resolve this inconsistency and predict a nearly linear geometry with an ∠Ag–O–Ag of 172°.[29] More broadly, CCSD(T)-predicted stabilities for various oxide and hydroxylated silver cluster ions show good agreement with signal strengths from mass spectra,[29,30] highlighting the reliability of this method in describing such systems.

In addition to the Ag-based clusters discussed above, silver hydride clusters (Ag_nH^+) have attracted considerable interest, and thus have been the focus of a number of experimental[27,45] and theoretical studies.[17,33,36,37,46] Among these ions, Ag_2H^+ holds great potential for applications in catalysis while it serves as the basis for the study of model reactions.[45,47] Most theoretical investigations using the DFT method predict that the ground-state geometry of Ag_2H^+ is bent, having C_{2v} symmetry with Ag–Ag bond lengths in the range of 2.8–3.0 Å.[36,37] This contrasts earlier HF calculations that predict a linear $D_{\infty h}$ geometry.[17] Subsequent CCSD calculations confirmed a bent ground-state geometry with an Ag–Ag bond length of approximately 3.0 Å.[46]

Using a generalized gradient approximation (GGA) functional (PW91PW91) within the DFT formalism, Zhao *et al.*[37] identified ground-state geometries, relative stabilities, and most favourable dissociation channels of Ag_nH^+ clusters noting clear differences in fragmentation profiles between silver clusters having odd and even numbers of atoms. The ground-state structures of larger Ag_nH^+ clusters in that study were determined by attaching H atoms to pre-optimized Ag_n^+ clusters. Although this method provides useful structural information, incorporating a global minimum search would have been advantageous for larger clusters with complex potential energy surfaces, ensuring that low-energy and structurally diverse isomers are fully captured.[48] Furthermore, significant discrepancies in the predicted dissociation energies, particularly for the Ag_nH^+ clusters with an even number of Ag atoms, are observed when comparing results obtained using the GGA functional[37] with those from hybrid-B3LYP functional/MP2 treatments.[36] This method dependence warrants reinvestigation of the dissociation energies of Ag_nH^+ clusters using more accurate approaches such as CCSD(T).

A property that depends on the size and structure of the ions and can be easily probed experimentally is their electrical mobility, which is related to their collision cross section (CCS).[49,50] Theoretical work by Jarrold and co-workers has demonstrated that CCS (and thus the electrical mobility of the clusters) can be predicted using cluster geometries determined by quantum chemical simulations.[51]

Comparison of theoretically predicted and experimentally determined CCSs can serve as a means for validating geometries obtained from *ab initio* methods. Weis *et al.*[35] used a pulsed laser vaporization source and a drift tube to determine the electrical mobility, and thus the CCS of pure silver cluster cations (Ag_n^+). They reported good agreement between measured and computed CCSs, although a few notable deviations were observed for specific clusters. More recently, Maisser *et al.*[52] employed a Differential Mobility Analyzer (DMA) to measure the electrical mobilities of silver-containing clusters generated by spark ablation under atmospheric conditions. Subsequent measurements showed that apart from the pure silver ions, their oxidized, hydroxylated, and potentially hydrogenated variants existed in the resulting aerosol plumes.[53] Using rigorously optimized structures and the trajectory method to determine the CCS of Ag-based clusters, several previously unassigned peaks in the mobility spectra reported by Maisser *et al.*[52] were attributed to specific oxidized ($Ag_nO_k^+$; n = 1–4 and k = 1–5) and hydroxylated ($AgO_kH_m^{\pm}$; k, m = 1–4) cluster ions.[29,30] Interestingly, while most spectral features of experimental mobility are now matched to known cluster types, some others still remain unassigned. These likely correspond to other ionic species, including Ag_nH^+ clusters, as suggested by Maisser *et al.*[53] Theoretical mobility predictions for these species could therefore help the interpretation of the experimental electrical mobility distributions of silver aerosol clusters, produced by atmospheric-pressure spark ablation.

As previously reported by Maisser *et al.*, cationic silver hydrides (Ag_nH^+) are among the products formed during atmospheric-pressure spark ablation of silver.[53] A distinct odd–even alternation in the mass spectra of Ag_nH^+ clusters, with clusters having an even number of Ag atoms (denoted as "even-n Ag_nH^+") exhibiting significantly stronger signals than their odd-numbered counterparts (denoted as "odd-n Ag_nH^+"), indicating that the former are thermodynamically more stable and thus more abundant. Although Zhao *et al.*[37] theoretically also predicted an odd–even alternation in the stabilities of Ag_nH^+ clusters, subsequent comparisons have shown significant discrepancies among different DFT functionals in predicting both geometries and stabilization energies, as discussed earlier. These inconsistencies highlight the need for a more accurate and comprehensive explanation. Moreover, their thermal properties and electrical mobility have not been thoroughly investigated.

Here we theoretically predicted the equilibrium geometries and stabilities of low-energy isomers of Ag_nH^+ clusters, where n ranges from 1 to 7. We compared the calculated stabilization energies and mobilities of these clusters with experimentally determined mass and electrical mobility spectra.[52,53] We used the highly accurate CCSD(T) level of theory and *ab initio* molecular dynamics (AIMD)[54] to determine, respectively, the electronic energies and the thermal stabilities of these clusters. Additionally, we provided further insights into the nature of bonding in the Ag_nH^+ clusters using frontier molecular orbitals (FMO),[55] natural bond orbital (NBO),[32] molecular electrostatic potential (MESP),[56,57] quantum theory of atoms in molecules

(QTAIM),[58,59] and non-covalent interaction (NCI)[60] analysis. The structure of the rest of the paper is as follows: Section 2 describes the computational methods employed, Section 3 presents our results, and Section 4 summarizes the key conclusions.

2 Computational details

2.1 Electronic structure

The computational approach adopted in this work closely follows the methodologies described in our earlier studies on silver oxide cations[29] and hydroxylated silver ion clusters.[30] Initial candidate structures of Ag_nH^+ clusters were generated using the ABCluster program, which is based on the artificial bee colony algorithm for global minimum searches.[61–63] Following this, full-dimensional geometry optimizations were carried out on all candidate structures using the hybrid meta-GGA M06 functional[64] with split-valence triple-ζ basis set that includes polarization functions (6-311G(d,p)) for the H atom (contracted to 3s1p)[65] and the Stuttgart/Dresden effective core potential (SDD) and corresponding ECP28MWB basis set for the Ag atoms (contracted to 6s5p3d).[66] Theoretically predicted properties of pure ionic silver clusters (Ag_n^+, where n = 2–22) obtained from *ab initio* calculations using the M06 functional in conjunction with the above-mentioned basis sets were reported to be consistent with the experimental observations.[14] We should note here that the M06 functional is capable of identifying the low-energy isomers of charged silver clusters,[40] and was used to determine energy differences among these isomers that were in excellent agreement with CCSD(T) predictions (within $\pm$0.1 eV).[67]

After identifying several low-energy isomers of a specific Ag_nH^+ cluster at the M06 level, we further optimized their geometries at the CCSD level of theory[42–44] using the same basis sets as mentioned above. In the CCSD geometry optimization step, we considered all potential isomers whose ground-state electronic energies were within 1.0 eV of the lowest-energy isomer determined at the M06 level for each Ag_nH^+ cluster. For all the cases, we considered the two lowest spin states: singlet and triplet for clusters with an even number of electrons, and doublet and quartet for those with an odd number. We performed harmonic vibrational frequency calculations at the DFT level to ensure that the geometries optimized at the CCSD level corresponded to local minima on the potential energy surfaces. All geometry optimization and vibrational frequency calculations were performed using the Gaussian 16 program.[68]

Single-point energy calculations were carried out using the CCSD(T) method on the geometries optimized by CCSD to determine the ground-state electronic energies of the Ag_nH^+ clusters. For the CCSD(T) calculations, we used Dunning's augmented correlation-consistent triple-ζ basis sets for both H and Ag atoms, *viz.*, the aug-cc-pVTZ[69,70] (contracted to 4s3p2d) for H, and the cc-pVTZ-PP[71] (contracted to 5s5p4d2f1g) for Ag. Scalar-relativistic effects for Ag were treated using the cc-pVTZ-PP pseudopotential, whereas vector-relativistic (spin–orbit coupling) effects were not included explicitly.

The CCSD(T) method is often regarded as the "gold standard" in quantum chemistry for ground-state wavefunctions that predominantly have single-reference characters.[72] To examine the multireference nature in the ground state wavefunctions of these cationic clusters, we determined the T_1 diagnostics values from the CCSD(T) calculations, and found them to be below 0.017 for singlet spin states and under 0.026 for higher spin states, indicating a predominantly single-reference nature for all clusters we studied.[73,74] The CCSD(T) calculations were performed using the MOLPRO software suite.[75,76]

The stabilization energy (ΔE) of the Ag_nH^+ clusters is defined as the zero-point vibrational energy (ZPVE) corrected energy difference between the ionic cluster and the products of its unimolecular dissociative reaction. Since multiple dissociation channels (DCs) can exist, ΔE was calculated with respect to the lowest energy dissociation channel (LEDC), which is the pathway that requires the least amount of energy to dissociate or to release the largest amount of energy. Accordingly, for LEDC, ΔE is minimum among all DCs in the following expression:

$$\Delta E = E(Ag_aH_b)^+ + E(Ag_cH_d) - E(Ag_nH)^+. \quad (1)$$

Here, $E(Ag_nH)^+$, $E(Ag_aH_b)^+$ and $E(Ag_cH_d)$ are the ZPVE-corrected total energies of Ag_nH^+, $Ag_aH_b^+$, and Ag_cH_d clusters, respectively. Integers a and c must satisfy the constraint $a + c = n$, with $a \neq 0$, while either b or d can take the value of 1, but not simultaneously. Finally, the vertical electron affinity (VEA) and adiabatic electron affinity (AEA) of these cationic clusters were obtained as energy differences between the cation and its neutral counterpart, evaluated at the cation geometry (VEA) and at the optimized geometries of both species (AEA), respectively.

2.2 *Ab initio* molecular dynamics (AIMD)

To assess the thermodynamic stability of Ag_nH^+ clusters, AIMD simulations were carried out using the ωB97XD long-range corrected hybrid functional[77] and the def2-TZVP basis set within an NVT ensemble. The long-range corrected ωB97XD functional was selected because it explicitly accounts for long-range exchange and dispersion interactions, both of which can be important in coinage-metal clusters and metal-hydride systems. Benchmark studies indicate that ωB97XD can reproduce reasonable structural and energetic trends for systems involving transition-metal coordination and non-covalent interactions, compared with CCSD(T) reference data.[78]

AIMD simulations were run at 298 K, maintaining the temperature of the cluster using the Nosé–Hoover chain thermostat.[79,80] The velocity Verlet algorithm was used to propagate nuclear positions with a 0.5 fs timestep for a total duration of 20 ps. These simulations were carried out using the ORCA software package.[81]

Structural dynamics were analyzed by calculating the root mean square bond length fluctuation, defined as:[82]

$$\delta = \frac{1}{M}\sum_{i<j}^{n} \frac{\sqrt{\langle r_{ij}^2\rangle_t - \langle r_{ij}\rangle_t^2}}{\langle r_{ij}\rangle_t}, \quad (2)$$

where r_{ij} represents the bond length between the i-th and j-th atoms, M is the number of such ij pairs, and $\langle \ldots \rangle_t$ denotes the

time average over the entire simulated trajectory. Values of δ were calculated for all bonds (δ_{RMS}), only Ag–Ag bonds ($\delta_{RMS/Ag-Ag}$), and only Ag–H bonds ($\delta_{RMS/Ag-H}$).

2.3 Collision cross section and electrical mobility

The CCSs (Ω) and the electrical mobilities (Z) of the Ag_nH^+ clusters were calculated by the trajectory method (TM)[51] using the IMoS package developed by Larriba-Andaluz *et al.*[83,84] The TM is considered to be more accurate than other methods for determining electrical mobilities, such as the projection approximation or exact hard-sphere scattering methods, as it accounts for ion-gas interactions through a 12-6 Lennard-Jones (LJ) potential.[51] Helium was used as the carrier gas for all CCS and mobility calculations in this study to enable direct comparison with the experimental results provided by Maisser *et al.*[52] The LJ parameters for Ag–He and H–He interactions were chosen to be the same as in our earlier work on $AgO_kH_m^{\pm}$ clusters,[30] and were determined by fitting theoretical CCS predictions to measurements using drift tubes.[85,86] The Z values of the Ag_nH^+ clusters were determined as:[51]

$$Z = \left(\frac{\pi}{8k_BT}\right)^{1/2}\left[\frac{1}{m}+\frac{1}{m_B}\right]^{1/2}\frac{3ze}{4N\Omega}. \quad (3)$$

Here, m and m_B are, respectively, the masses of the Ag_nH^+ cluster and of the He atom, z is the number of elementary charges (considered to be unity in all our calculations), e is the elementary charge (1.602177×10^{-19} C), k_B is the Boltzmann constant (1.380649×10^{-23} J K^{-1}), T is the effective temperature (298 K), and N is the number density of the gas at 1 atm pressure.

2.4 Interatomic interactions

To gain insight into the interatomic interactions and bonding nature in the Ag_nH^+ clusters, we performed a series of electronic structure analyses including FMO,[55] NBO,[32] QTAIM,[58,59] MESP,[56,57] and NCI.[60] The required density matrices for these analyses were obtained using the long-range corrected ωB97XD functional[77] at the DFT level, employing the same basis sets that were used for the CCSD(T) calculations. We should note here that we performed these analyses only for the lowest-energy isomer of each Ag_nH^+ cluster.

The FMO analysis, corresponding to the highest occupied molecular orbital (HOMO) and lowest unoccupied molecular orbital (LUMO), is used to assess the chemical reactivity of the charged clusters. According to Koopmans' theorem,[87] the ionization potential (IP) and electron affinity (EA) of chemical systems can be approximated from the energies of HOMO and LUMO, respectively, *i.e.*, $-\varepsilon_{HOMO}$ = IP and $-\varepsilon_{LUMO}$ = EA. These values can be used to derive conceptual DFT (CDFT) descriptors, such as chemical hardness (η = 1/2(IP − EA)),[88] chemical potential (μ = −1/2(IP + EA)),[88] and electrophilicity index ($\omega = \mu^2/2\eta$).[89] These descriptors, along with the HOMO–LUMO energy Gap (HLG), provide valuable information about the reactivity and the stability of the clusters. Specifically, larger η and HLG values indicate a more stable, less reactive species,[90] while μ and ω characterize the tendency of electrons to escape from a chemical system at equilibrium or accept electrons.[89]

NBO analysis was used to quantify donor–acceptor (D–A) interaction energies ($E^{(2)}$) within the clusters through second-order perturbation theory as:[32]

$$E^{(2)} = q_i\frac{|\mathbf{F}_{i,j}|^2}{\varepsilon_j-\varepsilon_i}, \quad (4)$$

where q_i is the donor orbital occupancy, $\mathbf{F}_{i,j}$ represent the off-diagonal Fock matrix elements, whereas ε_i and ε_j are the diagonal elements of the density matrix that represent the orbital energies. The presence of resonance structures was investigated using Natural Resonance Theory (NRT),[91] with the resonance hybrid defined as:

$$\Gamma_{NRT} = \omega_I\Gamma_I + \omega_{II}\Gamma_{II} + \omega_{III}\Gamma_{III} + \ldots, \text{ with } \sum\omega_\alpha = 1. \quad (5)$$

Here, Γ_I, Γ_{II}, Γ_{III}, … are the individual localized resonance structures having non-negative weights ω_I, ω_{II}, ω_{III}, …, respectively. Natural population analysis (NPA)[92] was performed to evaluate the atomic charges. All NBO, NRT, and NPA calculations were carried out using the NBO 7.0 software.[93]

Topological analysis of electron density was conducted using the QTAIM method,[58,59] which identifies bond critical points (BCPs) where the gradient of electron density is zero, *i.e.*, $\nabla\rho(\mathbf{r}) = 0$.[94,95] Covalent bonds are typically characterized by a high electron density $\rho(\mathbf{r})$ ($\geq$0.1 a.u.) and negative values of $\nabla^2\rho(\mathbf{r})$, whereas ionic bonds, hydrogen bonds, and van der Waals interactions exhibit positive values of $\nabla^2\rho(\mathbf{r})$ at the BCP.[96] Additionally, the ratio of kinetic energy density $G(\mathbf{r})$ to potential energy density $V(\mathbf{r})$ can further be used to classify the nature of interactions. Specifically, a ratio $G(\mathbf{r})/|V(\mathbf{r})|$ higher than unity suggests a non-covalent interaction, whereas a value less than 0.5 indicates covalent bonding.[59] Other topological descriptors, such as electron localization function (ELF)[97,98] and localized-orbital locator (LOL),[99] can also provide insights into the nature of chemical bonding in a molecular system. If the values of these descriptors approach unity at the BCP, the interaction can be regarded as covalent. Conversely, non-covalent interactions usually yield ELF and LOL values of less than 0.5. Finally, NCI plots based on the Reduced Density Gradient (RDG) were generated to identify and characterize weak interactions.[60] All QTAIM and NCI analyses were performed using the Multiwfn package.[100]

3 Results and discussion

3.1 Structure

The ground state geometries of the lowest-energy isomer of the Ag_nH^+ clusters are illustrated in Fig. 1. Isomers with ZPVE-corrected relative energies within 1.0 eV of the lowest-energy isomer (designated as isomer (I)) for each cluster with n Ag atoms are shown in Fig. S1–S4 of the SI. The optimized atomic coordinates for all isomers are also provided in the SI (Table S1). Various electronic properties, including the relative total energy of

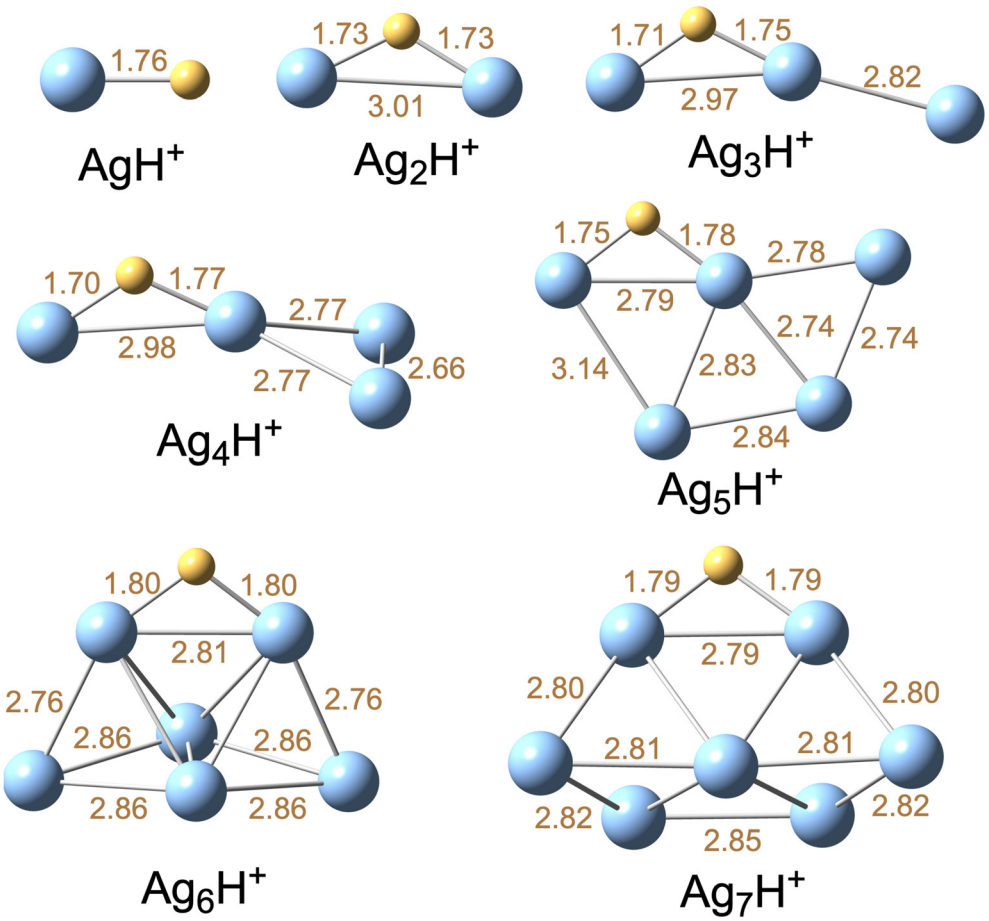

Fig. 1 Ground state structures of the lowest-energy isomer (I) of the Ag_nH^+ clusters, where n = 1–7, optimized at the CCSD level. Bond lengths are given in Ångstroms.

each isomer, VEA, and AEA, as well as stabilization energy along the LEDC, are summarized in Table 1.

We identify two low-lying isomers of Ag_3H^+ and four for Ag_5H^+, Ag_6H^+, and Ag_7H^+, all with ZPVE-corrected energies within 1 eV of the respective isomer (I). All the low-lying isomers are labeled sequentially with Roman numerals from (I) to (IV), based on ascending energy. C_{2v} and C_s are the most abundant symmetries among all the isomers of the Ag_nH^+ clusters. Notably, Ag_6H^+ has the largest number of symmetric isomers (in terms of total number of symmetry operations), featuring two isomers belonging to the C_{2v} and C_s point groups. Interestingly, each of the Ag_7H^+ isomers exhibits C_s point group symmetry. Among the larger clusters, at least two planar geometries are predicted among the isomers of the Ag_5H^+ cluster, while both Ag_6H^+ and Ag_7H^+ have one planar isomer each.

Consistent with previous findings for $AgO_kH_m^{\pm}$ clusters,[30] the Ag_nH^+ clusters favor low-spin states, *i.e.*, singlet and doublet states for even and odd numbers of electrons in the clusters, respectively. All low-lying isomers identified in this study also exhibit a preference for low-spin states, and are in contrast with predictions for the $Ag_nO_k^+$ clusters that predominantly exhibit high-spin states.[29] The low-spin preference of the Ag_nH^+ clusters aligns with similar trends reported for the pure Ag_n^+ clusters.[14] Along those lines, the structures of Ag_nH^+ clusters can also be viewed as hydrogen-capped Ag_{n-1}^+ clusters.[36]

At least two low-lying isomers exist for the larger clusters (*i.e.*, Ag_5H^+, Ag_6H^+, and Ag_7H^+) that have a very small electronic energy difference ($\leq$0.16 eV) compared to their respective lowest energy isomer (I). Interestingly, the first two isomers of Ag_5H^+, *i.e.*, isomer (I) and isomer (II), can be considered quasi-degenerate since their ZPVE-corrected electronic energy is almost identical (see Table 1). Similarly, (I) and (II) isomers of Ag_6H^+ can also be treated as degenerate. Therefore, these low-lying isomers of the Ag_nH^+ clusters could be thermally accessible at ambient conditions.

A consistent structural feature predicted for Ag_nH^+ clusters with $n \geq 2$ is the bonding of the H atom to at least two neighbouring Ag atoms in all identified isomers (see Fig. 1 and Fig. S1–S4 in the SI). In certain low-lying isomers, specifically Ag_5H^+ (IV), Ag_6H^+ (II), and all Ag_7H^+ isomers except (I), the H atom is coordinated to three Ag atoms. The Ag–H bond lengths exhibit systematic differences depending on coordination. In bi-coordinated isomers, the Ag–H bond lengths fall within the range of 1.70–1.80 Å. In contrast, the tri-coordinated H atom isomers show slightly elongated Ag–H bonds (1.82–2.00 Å).

Table 1 Summary of the results from the CCSD(T) calculations on the ground state of Ag_nH^+ clusters. Key: Isomer refers to the isomer number of the Ag_nH^+ clusters; PG is the point group symmetry; E is the energy (in eV) of a isomer with respect to lowest-energy isomer; VEA is the vertical electron affinity (in eV); AEA is the adiabatic electron affinity (in eV); Ω is the collision cross section (in Å^2) in He; Z^{-1} is the inverse electrical mobility (in V s m^{-2}) in He; LEDC is the lowest energy dissociation channel; ΔE is the zero-point vibrational energy corrected stabilization energy (in eV) for the lowest energy isomer with respect to LEDC

Species	Isomer	PG	E	VEA	AEA	Ω	Z^{-1}	LEDC	ΔE				
AgH^+	I	$C_{\infty v}$	—	9.15	9.24	27.22	457.17	$Ag^+ + H$	0.41[a]	0.38[b]	—	—	—
Ag_2H^+	I	C_{2v}	—	5.58	5.59	33.96	575.40	$Ag^+ + AgH$	2.24[a]	2.43[b]	2.34[c]	2.14[d]	2.08[e]
Ag_3H^+	I	C_s	—	6.18	6.45	43.60	741.03	$Ag + Ag_2H^+$	1.02[a]	1.18[b]	1.11[c]	—	—
	II	C_{2v}	0.25	6.46	6.69	41.25	701.17						
Ag_4H^+	I	C_s	—	4.72	5.57	50.18	854.26	$Ag_3^+ + AgH$	1.60[a]	1.71[b]	1.45[c]	1.28[d]	1.17[e]
Ag_5H^+	I	C_s	—	6.24	6.97	54.71	932.14	$Ag + Ag_4H^+$	0.97[a]	1.22[b]	1.28[c]	—	—
	II	C_s	0.01	5.91	6.98	56.89	969.33						
	III	C_s	0.16	5.38	7.16	58.02	988.65						
	IV	C_{2v}	0.28	6.44	7.32	55.33	942.79						
Ag_6H^+	I	C_{2v}	—	5.48	5.58	57.33	977.34	$Ag_5^+ + AgH$	1.93[a]	2.26[b]	1.74[c]	1.21[d]	2.01[e]
	II	C_{2v}	0.08	4.91	5.70	60.04	1023.59						
	III	C_s	0.12	5.39	5.71	60.00	1023.02						
	IV	C_s	0.55	4.30	6.14	67.45	1149.91						
Ag_7H^+	I	C_s	—	5.80	5.93	62.52	1066.31	$Ag + Ag_6H^+$	1.56[a]	1.73[b]	1.67[c]	—	—
	II	C_s	0.12	6.01	6.06	60.37	1029.71						
	III	C_s	0.14	5.88	6.08	60.05	1024.20						
	IV	C_s	0.75	5.73	6.71	66.80	1139.37						

[a] CCSD(T)/cc-pVTZ-PP (Ag)/aug-cc-pVTZ (H) calculations (this work). [b] ωB97XD/cc-pVTZ-PP (Ag)/aug-cc-pVTZ (H) calculations (this work). [c] PW91PW91/LANL2DZ (Ag)/6-311++G(d,p) (H) calculations.[37] [d] B3LYP/LANL2DZ (Ag)/6-31G(d) (H) calculations.[36] [e] MP2/LANL2DZ (Ag)/6-31G(d) (H) calculations.[36]

Among tri-coordinated H atom isomers, two Ag–H bonds (1.82–1.89 Å) are typically shorter compared to the third one (1.96–2.00 Å).

Considering only the lowest-energy isomers (I), the Ag–H bond in AgH^+ (1.76 Å) is slightly longer than the two equivalent Ag–H bonds in Ag_2H^+ (1.73 Å). The Ag_2H structural motif present in each Ag_nH^+ cluster for $n \geq 2$ nevertheless shows marked size-dependent variations. For example, the two Ag–H bonds in Ag_2H^+, Ag_6H^+ (1.80 Å), and Ag_7H^+ (1.79 Å) are very similar in length, whereas more pronounced differences between the two Ag–H bonds are observed for the remaining clusters. A similar trend appears in the Ag–H–Ag angle within the Ag_2H motif. In the smaller clusters (n = 2–4), this ∠Ag–H–Ag is noticeably larger (≈120°) than in the larger clusters (≈100°). Considering the overall cluster geometry, the Ag–Ag bond lengths are substantially longer, spanning 2.65–3.14 Å across all isomers, indicating a relatively extended metal framework.

We find good overall agreement for the even-n Ag_nH^+ clusters with the B3LYP-optimized structures reported by Khairallah and O'Hair,[36] although their geometries tend to overestimate both Ag–Ag and Ag–H bond lengths by about 0.05 Å. For Ag_6H^+, however, significant differences emerge. We identify isomer (I) as the structure with the lowest energy, whereas Khairallah *et al.* reported isomer (III) as the lowest with calculations at the B3LYP level. Our calculations show that the relative energy of isomer (III) is 0.12 eV above isomer (I), compared to ∼ 0.20 eV reported by Khairallah and O'Hair, even at the MP2 level using B3LYP-optimized geometries (see Fig. S5 in the SI). Likewise, they reported that isomer (II) lies ∼0.25 eV above isomer (I) at the MP2 level, whereas in our study, this difference is only 0.08 eV. Similar overall agreement is also found with the DFT results of Zhao *et al.*[37] for the smaller Ag_nH^+ clusters (n = 2–4). However, significant discrepancies arise in both the geometrical features and relative energies of the isomers for the larger clusters, particularly for Ag_5H^+–Ag_7H^+ (see Fig. S5 in the SI). Notably, the lowest-energy isomer (I) of Ag_7H^+ predicted in our work was not identified in their study, likely because in their approach, larger Ag_nH^+ structures were constructed by simply adding an H atom to pre-optimized Ag_n^+ clusters, rather than using a more exhaustive global minimum search.

3.2 Stability

For the lowest-energy isomer, the LEDC, along with the corresponding ZPVE-corrected stabilization energy (ΔE) for the Ag_nH^+ clusters, is reported in Table 1, while those for all other possible DCs are provided in Table S2 in the SI. As expected, the number of dissociation pathways increases with cluster size due to possible fragment combinations. A clear and systematic pattern is predicted in the LEDCs with the number of Ag atoms in the cluster. For the clusters with even values of n, the most favourable dissociation channel involves the loss of a neutral AgH unit, yielding a charged silver cluster fragment:

$$Ag_nH^+ \rightarrow Ag_{n-1}^+ + AgH$$

In contrast, for odd-n Ag_nH^+ clusters, the LEDC instead leads to the formation of a neutral Ag atom and a charged silver hydride fragment:

$$Ag_nH^+ \rightarrow Ag + Ag_{n-1}H^+$$

This trend in LEDC can be explained by examining the electronic structures of the resulting fragments. Specifically, the odd-numbered cationic fragments, which are produced from the dissociation of even-n Ag_nH^+ clusters, possess even numbers of

valence electrons. This results in a closed-shell electronic configuration, enhancing their stability.[14,37] Similarly, the even-$Ag_{n-1}H^+$ fragments formed from the dissociation of odd-n Ag_nH^+ clusters also exhibit closed-shell valence electron configurations, contributing to their overall stability. Therefore, in both cases, the Ag_nH^+ clusters preferentially dissociate into fragments having closed valence shells.

The CCSD(T) calculated ΔE values for the lowest-energy isomer of Ag_nH^+ clusters with respect to LEDC are reported in Table 1. A distinct alternating pattern of peaks and troughs is evident (see Fig. 2(a)). The even-n Ag_nH^+ clusters exhibit significantly higher stabilization energies, ranging from 1.60 to 2.24 eV, compared to the odd-n Ag_nH^+ clusters that have values between 0.41 and 1.56 eV. As mentioned above, the predicted stabilities of the Ag_nH^+ clusters can be explained by their corresponding valence electron configurations. The even-n Ag_nH^+ clusters possess closed-shell configurations, which result in greater ΔE values. Conversely, the open-shell configurations of the Ag_nH^+ clusters with odd n lead to lower stabilization energies. Similar odd–even alternation in ΔE is also observed for the ωB97XD calculations (see Table 1). However, the ΔE values obtained using the ωB97XD functional systematically overestimate the CCSD(T) stabilization energies by approximately 0.11–0.33 eV, with the exception of AgH^+.

The signal strength in the experimentally determined mass spectra serves as an important indicator of relative abundances and, consequently, may relate to the stabilities of the clusters (see Fig. S6 in the SI). Therefore, we can qualitatively compare the mass spectral signals with the theoretically calculated stabilization energies. However, to account for the mass-dependent transmission of the spectrometer, the measured mass spectral intensities of the clusters were corrected using a skew-log-normal envelope function, which provides a better description of the asymmetric transmission profile. The envelope was parameterized using experimental transmission data reported by Schmidt-Ott *et al.*,[101] while the explicit functional form, optimized parameters, and fit quality are provided in the SI (see Table S3 and Fig. S7). The corrected intensities as reported by Maisser *et al.*[53] were subsequently normalized to the strongest signal (Ag_2H^+). Both measured and corrected spectra exhibit similar overall profiles (see Fig. 2(a) and Fig. S8 in the SI), although the corrected spectra show systematically enhanced intensities for $n \geq 4$. Likewise, the calculated stabilization energies were normalized to the cluster with the largest ΔE value (Ag_2H^+) and directly compared to the normalized experimental mass spectra in Fig. 2(a).

The theoretically calculated ΔE values along the LEDC pathway show good overall agreement with the corresponding signal strengths of the Ag_nH^+ clusters in the mass spectra. Notably, the similar odd–even alternation in signal strength is observed for n = 1 to 5, supporting the theoretical predictions, but not for $n \geq 6$. At larger cluster sizes (n = 6–7), however, the measured abundances remain somewhat suppressed despite the transmission correction, whereas the calculations still predict comparatively larger stability and preserve the odd–even alternation. These discrepancies could be due to fragmentation during the

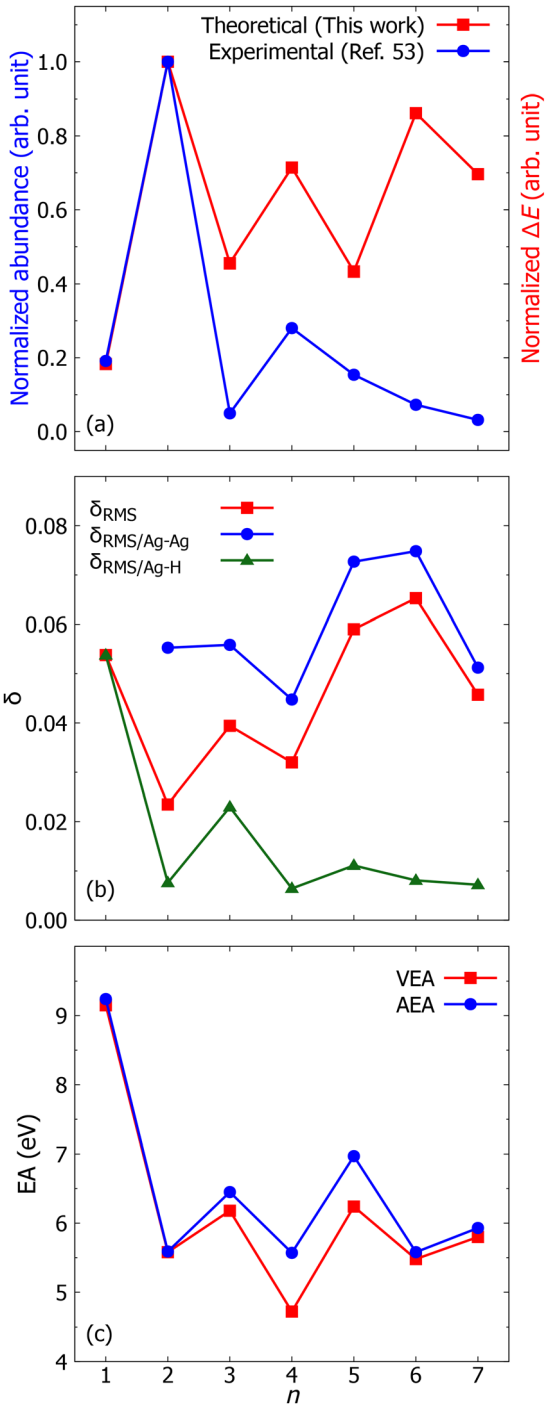

Fig. 2 (a) Normalized stabilization energies (ΔE) of the Ag_nH^+ clusters computed using the CCSD(T)/cc-pVTZ-PP (Ag)/aug-cc-pVTZ (H) level, compared with experimental abundances from mass spectrometry by Maisser *et al.* (ref. 53). Experimental data are corrected using a skew-log-normal envelope function. All values are normalized to their respective maxima (Ag_2H^+). (b) Root mean square bond length fluctuations for Ag–H ($\delta_{RMS/Ag-H}$), Ag–Ag ($\delta_{RMS/Ag-Ag}$), and all bonds (δ_{RMS}) in the lowest-energy isomers of Ag_nH^+ clusters, obtained from AIMD simulations at 298 K using the ωB97XD/def2-TZVP method. (c) Adiabatic (AEA) and vertical (VEA) electron affinities (in eV) of the lowest-energy isomers of Ag_nH^+ clusters calculated by the CCSD(T)/cc-pVTZ-PP (Ag)/aug-cc-pVTZ (H) level.

measurements, limited cluster growth under experimental conditions, or limitations of the theoretical model employed here, such as the absence of kinetic models.

A similar odd–even alternation in stabilization energies was also reported by Zhao *et al.*[37] using GGA functionals (see Table 1). However, their ΔE values are consistently either higher or lower compared to our CCSD(T) results, with deviations reaching up to 0.31 eV for the Ag_5H^+ cluster (see Fig. S9 in the SI). Likewise, both B3LYP and MP2 calculations mostly underestimate stabilization energies compared to the CCSD(T) results, with differences ranging from 0.10 to 0.72 eV and from 0.08 to 0.43 eV, respectively.[36] Despite these variations in absolute values, the predicted LEDC channels are consistent across studies, with both Zhao *et al.* and Khairallah *et al.* indicating the same channels as identified in our work.

The structural rigidity of Ag_nH^+ clusters was assessed through the computed root mean square bond length fluctuations (δ). For each cluster, δ was evaluated considering all bonds (δ_{RMS}), only Ag–Ag bonds ($\delta_{RMS/Ag–Ag}$), and only Ag–H bonds ($\delta_{RMS/Ag–H}$) (see Fig. 2(b); additional results for all low-lying isomers are provided in Fig. S10–S13 in the SI). According to the Lindemann criterion,[102,103] values of δ below 0.1 are indicative of solid-like clusters with rigid, well-defined structures, while values above 0.2 correspond to liquid-like behavior, and $\delta \approx 0.15$ is generally considered as the onset of structural disorder. All Ag_nH^+ isomers studied here exhibit δ_{RMS} values below 0.15, demonstrating that they remain structurally rigid at 298 K. Importantly, since smaller δ values reflect greater resistance to thermal distortion and therefore higher stability,[104] δ provides qualitative insight into relative stabilities of the clusters. Indeed, the predicted variations in δ_{RMS} are consistent with the computed stabilization energies (ΔE), both displaying a pronounced odd–even alternation. Specifically, for n = 1–5, odd-numbered clusters exhibit larger δ_{RMS} values, suggesting enhanced structural flexibility and correspondingly lower thermodynamic stability relative to their even-numbered counterparts.

Analyzing the bond-specific contributions to δ_{RMS}, it is evident that for all lowest-energy isomers, the root-mean-square fluctuation associated with Ag–H bonds ($\delta_{RMS/Ag–H}$) is consistently lower than that for Ag–Ag bonds ($\delta_{RMS/Ag–Ag}$). This indicates that Ag–Ag bonds are generally more flexible, whereas Ag–H bonds provide greater structural rigidity. The enhanced stability of the Ag–H bonds is discussed in detail in Section 3.4. The AgH^+ cluster displays a significantly higher $\delta_{RMS/Ag–H}$ compared to other Ag_nH^+ species. This larger bond fluctuation correlates well with its relatively low ΔE and weak intensity in the mass spectrum, collectively indicating reduced thermodynamic stability. Among low-lying isomers of larger clusters, $\delta_{RMS/Ag–Ag}$ values are generally greater than $\delta_{RMS/Ag–H}$, reflecting the flexibility of the Ag framework (see Fig. S10–S13 in the SI). Exceptions include isomer (II) of Ag_6H^+ and isomers (III) and (IV) of Ag_7H^+, which exhibit comparatively greater $\delta_{RMS/Ag–H}$ values. Interestingly, in all these isomers, the H atom is coordinated to three Ag atoms.

The VEA and ZPVE-corrected AEA values of the lowest-energy isomers of the Ag_nH^+ clusters, calculated at the CCSD(T) level, are summarized in Table 1. The values clearly exhibit the distinct odd–even alternation, as previously observed in LEDC, signal strengths in mass spectra, and δ_{RMS} values (see Fig. 2(c)). odd-n Ag_nH^+ clusters generally show higher VEA and AEA values than their adjacent even-n Ag_nH^+ counterparts. The highest electron affinity is predicted for AgH^+, with VEA and AEA values of 9.15 and 9.24 eV, respectively, indicating a very high electron affinity of this cluster. In contrast, Ag_2H^+ has significantly smaller VEA and AEA values (5.58 and 5.59 eV, respectively). Similarly, isomer (I) of Ag_3H^+ and Ag_5H^+ have higher electron affinities compared to Ag_2H^+, Ag_4H^+, and isomer (I) of Ag_6H^+. This trend can be explained by the fact that electron attachment to odd-numbered Ag_nH^+ clusters, which are initially open-shell, results in stable closed-shell neutral clusters. Conversely, attaching an electron to even-n Ag_nH^+ clusters typically produces open-shell species, resulting in lower electron affinities.[67] We should note here that a similar odd–even alteration in the electron affinity values for pure silver clusters was also reported by McKee *et al.*[14]

3.3 Electrical mobilities

The CCSs, calculated by the TM method, and the resulting inverse electrical mobilities (Z^{-1}) for all isomers of Ag_nH^+ clusters are summarized in Table 1. The computed Z^{-1} values for Ag_nH^+ clusters and those of pure Ag_n^+ ions from Weis *et al.*[35] are labelled on the experimentally measured electrical mobility spectrum reported by Maisser *et al.*,[52] as illustrated in Fig. S14 of SI. Smaller clusters, such as AgH^+ and Ag_2H^+, exhibit relatively lower Z^{-1} values (457.17 and 575.40 V s m^{-2}, respectively), whereas a pronounced increase in Z^{-1} values, ranging from approximately 701.17 to 1149.91 V s m^{-2}, is observed as cluster size increases from Ag_3H^+ to Ag_7H^+.

The presence of multiple low-lying isomers for clusters containing three or more Ag atoms introduces complexity to the interpretation of the experimental electrical mobility spectrum. For instance, the Ag_3H^+ cluster has two energetically comparable isomers (I and II), whose calculated inverse mobilities differ by only about 40 V s m^{-2}, suggesting both isomers may populate the same peak of the experimental spectrum. This ambiguity in experimentally identifying isomers becomes more pronounced for the larger clusters. In particular, isomers (I) and (IV) of Ag_5H^+ and isomers (II) and (III) of both Ag_6H^+ and Ag_7H^+ differ in Z^{-1} values by less than 10 V s m^{-2}. Furthermore, the Z^{-1} value of isomer (I) of Ag_6H^+ differs by approximately 10 V s m^{-2} compared to isomers (II) and (III) of Ag_5H^+. Several other such pairs of closely spaced mobility values are also evident among different isomers of Ag_6H^+ and Ag_7H^+ clusters.

In Ag_5H^+, the lowest-energy isomer (Z^{-1} = 932 V s m^{-2}) and the quasi-degenerate isomer (Z^{-1} = 969 V s m^{-2}) differ in Z^{-1} values by $\sim$37 V s m^{-2}. Distinguishing between these species would require a resolving power of $\sim$26, which is well within reach of advanced commercial instruments such as the P5 parallel plate DMA or the half-mini DMA,[105] but remains challenging under typical measurement conditions. The limitation becomes more pronounced for the isomers (II) and (III) of Ag_6H^+, where Z^{-1} values differ by only $\sim$0.6 V s m^{-2}. Separating

these isomers would require a resolving power of around 1800, which is far beyond the capabilities of current DMA technology and, to our knowledge, not even achieved in low-pressure drift-tube or cyclic IMS systems, where the highest reported resolving powers barely exceed 1000.[106,107] These findings highlight that mobility measurements alone are rarely sufficient for unambiguous isomer resolution, emphasizing the role of theoretical calculations in supporting the interpretation of experimental spectra.

3.4 Interatomic interactions

The notably high stability of the Ag_2H^+ cluster, as previously discussed, can be interpreted from an FMO perspective. As shown in Fig. 3, the HOMO in Ag_2H^+ is formed by constructive orbital overlap involving the valence 5s and $4d_{xy}$ hybrid orbitals of the two Ag atoms and the 1s orbital of the H atom. Consequently, overcoming this strongly positive overlap to generate the most favourable dissociation products (AgH^+ + Ag) could require substantial energy, which leads to a relatively high ΔE value. The graphical representations of the HOMO and LUMO for the Ag_nH^+ clusters are depicted in Fig. S15–S21 in the SI, with their corresponding energies and HOMO–LUMO energy gap (HLG) values summarized in Table S4 in the SI. With the exception of AgH^+ and Ag_2H^+, the H atom does not contribute significantly to the formation of either the HOMO or LUMO. For clusters with $n \geq 3$, both HOMO and LUMO exhibit antibonding character and are predominantly composed of the 5s orbitals of Ag atoms.

In general, both the HLG and chemical hardness (η) values tend to decrease as the cluster size increases (see Fig. 4 and Table S4 in the SI), indicating that larger Ag_nH^+ clusters exhibit increased chemical reactivity. However, there are a few exceptions to this trend. For example, the Ag_4H^+ and Ag_6H^+ clusters exhibit slightly greater HLG and η values compared to their preceding clusters (Ag_3H^+ and Ag_5H^+, respectively), making them marginally less reactive. The higher reactivity of Ag_4H^+ relative to Ag_2H^+ has previously been demonstrated experimentally by Wang *et al.*[45] Further analysis of the LUMO energies (ε_{LUMO}) and electrophilicity index (ω) (see Fig. 4 and Table S4 in the SI) indicates that AgH^+ is the most effective electron acceptor among the Ag_nH^+ clusters investigated in this study. This is further supported by its comparatively higher VEA and AEA values, as discussed earlier. Lastly, the negative chemical potential (μ) values indicate that the Ag_nH^+ clusters, especially the smaller ones such as AgH^+ and Ag_2H^+, are resistant to loss of electrons (see Fig. 4).

The charge distribution within the Ag_nH^+ clusters can be intuitively visualized through MESP maps, as depicted in Fig. 5. These maps visually represent the variation of electrostatic potential across the molecular surface. Different electrostatic

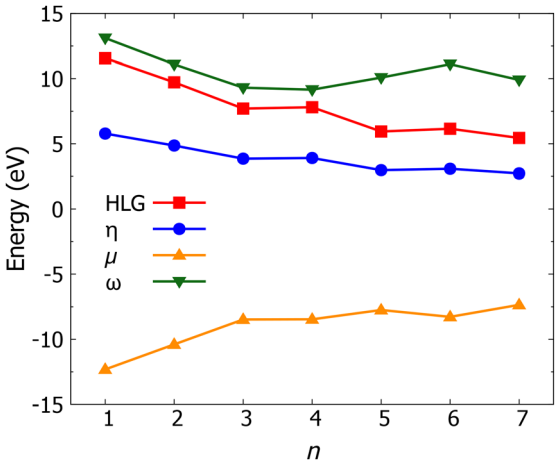

Fig. 4 HOMO–LUMO energy gap (HLG), chemical hardness (η), chemical potential (μ), and electrophilicity index (ω) of Ag_nH^+ (I) clusters (n = 1–7), obtained at the ω B97XD/cc-pVTZ-PP (Ag)/aug-cc-pVTZ (H) level of theory.

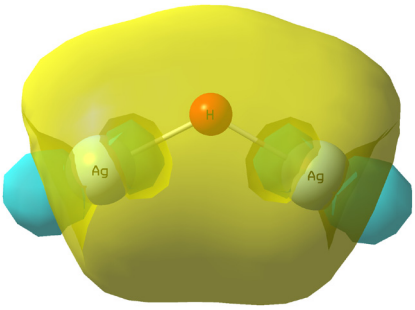

Fig. 3 HOMO of Ag_2H^+ cluster with isovalue of 0.02 obtained at the ωB97XD/cc-pVTZ-PP (Ag)/aug-cc-pVTZ (H) level of theory.

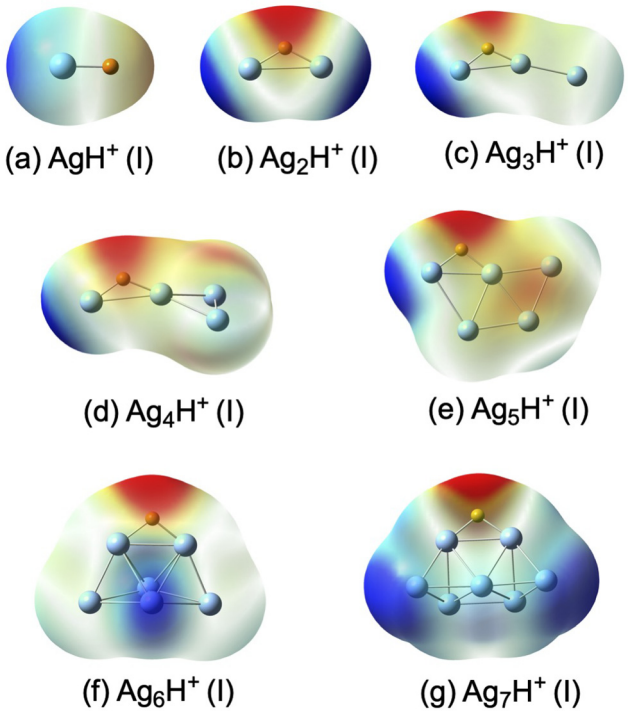

Fig. 5 MESP plots with isovalue 0.0004 a.u. of Ag_nH^+ (I) clusters (n = 1–7), obtained at the ωB97XD/cc-pVTZ-PP (Ag)/aug-cc-pVTZ (H) level of theory. Red areas indicate electron-rich environments, and blue areas indicate electron-deficient regions.

potential values are represented using a colour gradient: red < orange < yellow < green < blue. In this scale, red regions indicate low ESP and electron-rich areas, while blue regions correspond to high ESP and electron-deficient areas. The partial atomic charges of Ag_nH^+ clusters, derived using the NPA method, are provided numerically in Table S5 and visually illustrated in Fig. S22 in the SI. With the exception of the AgH^+ cluster, the H atom in all Ag_nH^+ clusters exhibits a partial negative charge, ranging from −0.57 to −0.66 a.u.

To assess the basis-set dependence of the negative charge on the H atom, additional NPA calculations were performed using the def2-TZVP basis set. The resulting H atom charges differ by less than 0.07*e* from those obtained with the aug-cc-pVTZ basis set for n = 2–7, indicating that the negative charge on the H atom is not sensitive to the choice of basis set (Table S5 in SI). Furthermore, the negatively charged H atom also has been reported for a wide range of transition-metal hydride cations, arising from metal-to-hydrogen charge transfer.[108–110] In contrast, the Ag atoms generally possess partial positive charges. In general, the MESP maps are in good agreement with the NPA-derived charge distributions, with the exception of the Ag_7H^+ cluster for which the most electrophilic region is not localized near the Ag atoms closest to the capped H atom.

In the AgH^+ cluster, the H atom is effectively neutral, with the positive charge localized almost entirely on the Ag atom. The lack of significant coulombic interaction between Ag and H atoms in this cluster may partially account for its relatively lower stability. In contrast, the Ag_2H^+ cluster exhibits strong Coulombic interactions, as both Ag atoms carry higher partial positive charges compared to other clusters, which are located near the H atom holding the most negative partial charge among all studied clusters. This pronounced electrostatic interaction likely contributes to the enhanced stability of the Ag_2H^+ cluster. A similar trend is observed for the larger clusters. The negatively charged H atom interacts electrostatically with the adjacent Ag atom(s) that carry the largest partial positive charges. Interestingly, the magnitude of partial positive charges on the Ag atoms diminishes progressively as their distance from the H atom increases in the larger Ag_nH^+ clusters. It is worth noting that the PW91PW91 calculated atomic charges on the H atom in these clusters, as reported by Zhao *et al.*,[37] are less negative than those obtained in this study.

Second-order perturbation theory within the NBO formalism provides a reliable method for estimating charge delocalization from Lewis-type (donor) to non-Lewis (acceptor) NBOs. The D–A interactions and their corresponding second-order perturbation energies ($E^{(2)}$) were systematically calculated for all lowest-lying Ag_nH^+ clusters. The most dominant D–A interactions, along with corresponding $E^{(2)}$ values, are summarized in Table S6 in the SI and are visually illustrated in Fig. 6 as well as in Fig. S23–S27 in the SI. With the exception of the smallest AgH^+ cluster, each investigated species exhibits at least one dominant D–A interaction. With the exception of Ag_7H^+, the clusters with even numbers of Ag atoms exhibit slightly higher $E^{(2)}$ values than their odd-numbered counterparts.

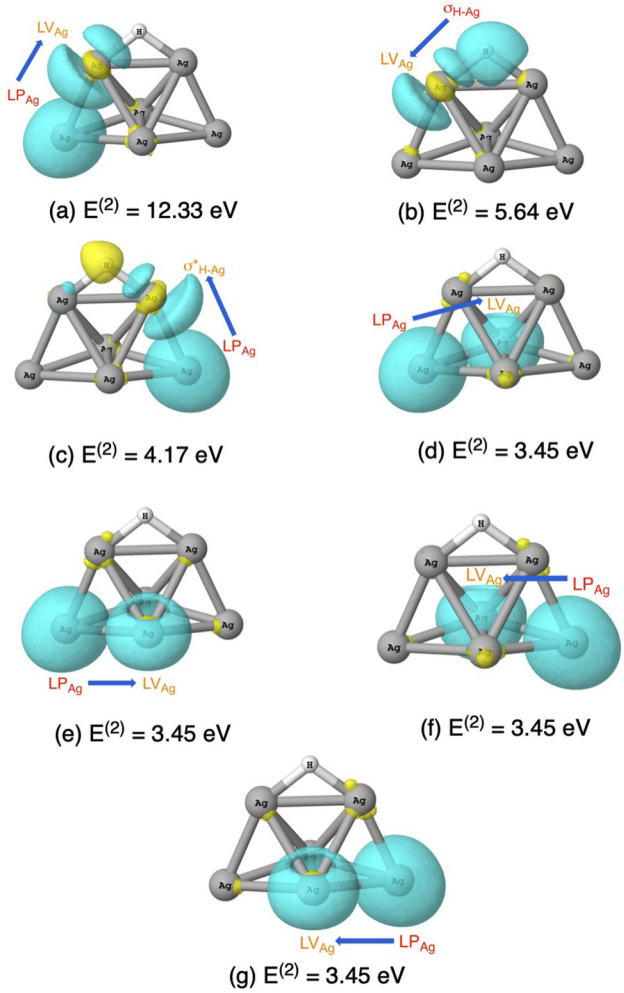

Fig. 6 Schematic representation of the most dominant donor–acceptor (D–A) interactions of the Ag_6H^+ (I) cluster with corresponding second-order perturbation energies ($E^{(2)}$'s). Here, σ_{H-Ag} is the H–Ag σ bonding NBO, σ^*_{H-Ag} is the H–Ag σ anti-bonding NBO, LP_{Ag} lone-pair NBO of Ag, and LV_{Ag} lone vacancy NBO of Ag. Calculations were performed at the ωB97XD/cc-pVTZ-PP (Ag)/aug-cc-pVTZ (H) level of theory.

For clusters with $n \leq 5$, the primary donor NBO is a σ bonding orbital (σ_{H-Ag} NBO), arising primarily from constructive overlap between the H 1s and Ag 5s orbitals. However, these σ_{H-Ag} NBOs have major contributions from the 1s orbital of the H atom with coefficients ranging between 82% and 90%, and a small contribution from the 5s orbital of Ag. For the Ag_2H^+, Ag_3H^+, and Ag_5H^+ clusters, the acceptor is an empty 5s orbital (lone vacant, LV_{Ag}, NBO) of a neighbouring Ag atom. In the case of Ag_4H^+, the acceptor is identified as an empty 3-center non-bonding (3Cn) NBO, composed of the 5s orbitals from three Ag atoms arranged in a triangular geometry opposite the H atom (see Fig. S25 in the SI). The formation of this 3Cn NBO involves destructive overlap between the 5s orbitals of two Ag atoms and the 5s orbital of the third Ag atom. In contrast, the corresponding bonding 3-center (3C) NBO involves the constructive orbital overlap among the 5s orbitals of all three Ag atoms (see Fig. S28 in the SI).

For larger clusters, *i.e.*, Ag_6H^+ and Ag_7H^+, multiple dominant D–A interactions are identified (see Fig. 6 here and Fig. S27 in the SI). Specifically, Ag_6H^+ has seven dominant D–A interaction pairs, while Ag_7H^+ has six. In these clusters, the primary donor NBOs are lone pairs (LP_{Ag}) localized on Ag atoms, primarily consisting of the 5s orbital. The acceptors are vacant valence 5s orbitals on nearby Ag atoms (LV_{Ag}). The LP_{Ag} orbitals are typically located on Ag atoms furthest from the H atom, and either they are neutral (Ag_6H^+) or they have minimal positive partial charges (Ag_7H^+). Additionally, in the Ag_7H^+ cluster, the lone pair on the negatively charged H atom can also act as a donor to the empty LV_{Ag} NBO of an adjacent Ag. The D–A interactions among various Ag atoms may contribute to electronic stabilization through charge delocalization, thereby enhancing the structural integrity of the metallic framework in these larger clusters.

The presence of these D–A pairs may give rise to multiple resonance structures, as shown in Fig. 7 here and Fig. S23–S27 in the SI. For Ag_2H^+, Ag_3H^+, and Ag_7H^+, two dominant resonance structures are identified. In contrast, three resonance structures are found for the Ag_4H^+ and Ag_5H^+ clusters. Notably, Ag_6H^+ exhibits six dominant resonance structures, which can be attributed to the numerous D–A interaction pairs in this system. Interestingly, all six resonance structures of Ag_6H^+ have nearly equal weights of approximately 10%.

The results from the QTAIM calculations are summarized in Table S7, whereas the corresponding BCPs are illustrated in Fig. S29 in the SI. Numerical values for each QTAIM descriptor, as discussed in Section 2.4, are provided for all relevant BCPs. No BCP is identified between the two Ag atoms coordinated to the same H atom, suggesting the absence of a direct bonding interaction between these Ag atoms within the QTAIM framework. In smaller clusters, such as AgH^+ and Ag_2H^+, the Ag-H BCPs exhibit relatively high electron densities ($\rho(\mathbf{r}) \approx 0.09$ a.u.) and $G(\mathbf{r})/|V(\mathbf{r})|$ ratios below 0.65, values that lie near the boundary between covalent and non-covalent bonding regimes. As the cluster size increases from Ag_3H^+ to Ag_7H^+, Ag–Ag BCPs begin to appear, but these are characterized by lower electron densities ($\rho(\mathbf{r}) \approx 0.03$–$0.04$ a.u.) and higher $G(\mathbf{r})/|V(\mathbf{r})|$ ratios (approaching or exceeding 0.80), consistent with non-covalent interactions. In contrast, the Ag–H BCPs in these clusters maintain higher electron densities ($\rho(\mathbf{r}) = 0.08$–0.10 a.u.) and lower $G(\mathbf{r})/|V(\mathbf{r})|$ ratios (0.63–0.68), reflecting stronger and more localized bonding. Consistent with these findings, the ELF and LOL values at Ag–H BCPs (ELF: 0.32–0.58; LOL: 0.40–0.51) are substantially greater than those at Ag–Ag BCPs (ELF: 0.12–0.19; LOL: 0.27–0.33), further supporting the interpretation that most Ag–Ag contacts in these Ag_nH^+ clusters are non-covalent in nature.

The nature of non-covalent interactions within the Ag_3H^+ to Ag_7H^+ clusters is further visualized through NCI isosurface plots (see Fig. S30 in the SI). These plots reveal only blue and red regions, corresponding to weakly attractive and repulsive interactions, respectively. The presence of blue regions between Ag atoms suggests weak but attractive non-covalent interactions, consistent with the low $\rho(\mathbf{r})$ and high $G(\mathbf{r})/|V(\mathbf{r})|$ values determined in the QTAIM analysis. These interactions may originate from D–A stabilization between the Ag atoms, as previously discussed within the context of NBO analysis, whereas the spatial extent of these attractive interaction regions increases with cluster size, becoming particularly pronounced in Ag_6H^+ and Ag_7H^+, where greater electron delocalization is expected. The absence of green isosurfaces indicates that van der Waals (dispersion) forces are not the dominant contributors. Therefore, the Ag–Ag contacts within these clusters are best described as weakly attractive and predominantly non-covalent.

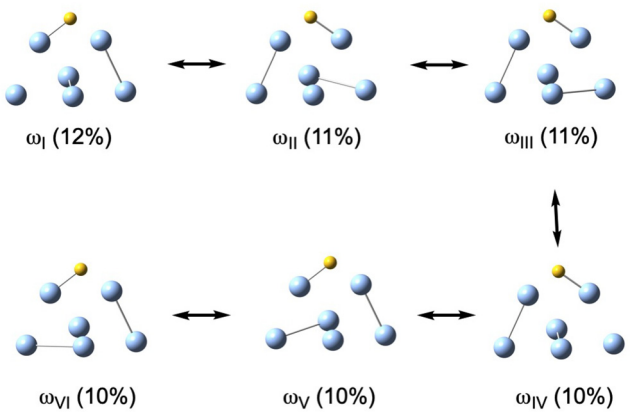

Fig. 7 Most dominant resonance structures of the Ag_6H^+ (I) cluster with corresponding weights (ω_i). Calculations performed at the ωB97XD/cc-pVTZ-PP (Ag)/aug-cc-pVTZ (H) level of theory.

4 Conclusions

We have carried out a comprehensive theoretical investigation on Ag_nH^+ clusters with n ranging from 1 to 7. The equilibrium geometries of low-lying isomers of the clusters were determined by highly accurate CCSD calculations for geometry optimization in combination with global minimum search strategies. Our results show a strong preference for low-spin (singlet/doublet) over high-spin states. In these clusters, the H atom bridges at least two Ag atoms *via* relatively short Ag–H bonds (1.70–2.00 Å), compared to relatively longer Ag–Ag bonds (2.65–3.14 Å). For larger clusters (Ag_5H^+, Ag_6H^+, and Ag_7H^+), quasi-degenerate isomers are identified, suggesting that multiple isomers may be thermally accessible under ambient conditions. Electrical mobilities of these ionic clusters were computed by the TM. These calculations show that different cluster sizes and Ag_nH^+ isomers can have similar mobilities, which cannot be easily resolved experimentally.

The ZPVE-corrected CCSD(T) calculations predict that Ag_2H^+ is the most stable species among the studied clusters, while the smallest AgH^+ is the least stable. A pronounced odd–even alternation in the predicted stability is observed, with even-n Ag_nH^+ clusters exhibiting enhanced stability due to their closed-shell electronic configurations. Similar odd–even alternation in hydrogen adsorption energies has also been reported

for other metal clusters (*e.g.*, Au,[111,112] Cu,[113] and Pd[114]), although the preferred parity (odd *vs.* even) depends strongly on the metal and on the binding mode (atomic H *vs.* molecular H_2). These Ag_nH^+ clusters preferentially dissociate into fragments (either Ag_{n-1}^+ or $Ag_{n-1}H^+$) that also have closed-shell electronic configurations. The computed stabilization energies show good qualitative agreement with signal intensities from mass spectra that reflect the stability of the clusters, both displaying the same odd–even alteration. The present coupled-cluster results reveal significant deviations from earlier DFT predictions in both geometries and relative stabilities, underlining the need for more robust *ab initio* methods.

AIMD simulations indicate that all low-energy isomers identified in this study remain well-defined and structurally rigid at room temperature, exhibiting a similar odd–even alternation in thermodynamic stability. For these clusters, Ag–Ag bonds are comparatively more flexible, whereas Ag–H bonds are shorter and more rigid. The enhanced rigidity of Ag–H bonds arises from strong Coulombic interactions between partially negatively charged H atoms and partially positive Ag atoms, as supported by NPA and MESP analyses. FMO analysis further indicates that chemical reactivity increases with cluster size, which is consistent with the narrowing of the HOMO–LUMO energy gap. With the exception of the AgH^+ cluster, second-order perturbation theory reveals numerous D–A interactions contributing to the overall stabilization of Ag_nH^+ clusters that may lead to resonating structures. For larger clusters, particularly Ag_6H^+ and Ag_7H^+, the D–A interactions between the Ag atoms likely enhance the stability of the metallic framework. Finally, QTAIM and NCI analyses show that Ag–Ag contacts are predominantly weak and non-covalent in nature, whereas Ag–H contacts are stronger and more localized, consistent with preceding analyses.

Overall, this study provides a systematic description of the structures, stabilities, bonding, and electrical mobilities of small Ag_nH^+ clusters based on high-level coupled-cluster theory. Apart from resolving inconsistencies in earlier DFT predictions and interpreting experimental measurements (mobility spectra), our results also elucidate the basis of odd–even stability patterns in metal-hydride clusters. These insights can provide a basis for designing advanced materials containing silver-based clusters for a wide range of applications.

Author contributions

S. B.: conceptualization, methodology, investigation, formal analysis, data curation, validation, writing – original draft, writing – review & editing, visualization. M. D. M.: investigation, data curation, visualization. A. M.: formal analysis, writing – review & editing. G. B.: conceptualization, supervision, formal analysis, funding acquisition, validation, writing – original draft, writing – review & editing, resources.

Conflicts of interest

There are no conflicts to declare.

Data availability

The supporting data has been provided as part of the supplementary information (SI). Supplementary information is available. See DOI: https://doi.org/10.1039/d5cp04890g.

Acknowledgements

This work was funded by the project ANCHOR (EXCELLENCE/0524/0307), which is implemented under the programme of social cohesion ''THALIA 2021-2027'' co-funded by the European Union, through the Research and Innovation Foundation of Cyprus. This work was also supported by the EMME-CARE project that has received funding from the European Union's Horizon 2020 Research and Innovation Program, under Grant Agreement No. 856612, as well as co-funding by the Government of the Republic of Cyprus. The authors thank the Cyclone High Performance Computing Facility of The Cyprus Institute for computational resources (Cyclone project number: pro24a04).

Notes and references

1 J. W. Alexander, *Surg. Infect.*, 2009, **10**, 289–292.
2 S. Medici, M. Peana, V. M. Nurchi and M. A. Zoroddu, *J. Med. Chem.*, 2019, **62**, 5923–5943.
3 M. Yusuf, in *Silver Nanoparticles: Synthesis and Applications*, ed. L. M. T. Martínez, O. V. Kharissova and B. I. Kharisov, Springer International Publishing, Cham, 2019, pp. 2343–2356.
4 Z. Chang, X. Jing, C. He, X. Liu and C. Duan, *ACS Catal.*, 2018, **8**, 1384–1391.
5 V. Bonacic-Koutecky, A. Kulesza, L. Gell, R. Mitric, R. Antoine, F. Bertorelle, R. Hamouda, D. Rayane, M. Broyer, T. Tabarin and P. Dugourd, *Phys. Chem. Chem. Phys.*, 2012, **14**, 9282–9290.
6 E. Coutiño-Gonzalez, W. Baekelant, J. A. Steele, C. W. Kim, M. B. J. Roeffaers and J. Hofkens, *Acc. Chem. Res.*, 2017, **50**, 2353–2361.
7 K. Oldenburg, K.-H. Meiwes-Broer and I. Barke, *Phys. Rev. Res.*, 2025, **7**, 023267.
8 E. Gwinn, D. Schultz, S. M. Copp and S. Swasey, *Nanomaterials*, 2015, **5**, 180–207.
9 M. Ganguly, C. Bradsher, P. Goodwin and J. T. Petty, *J. Phys. Chem. C*, 2015, **119**, 27829–27837.
10 X. Liu, T. Ki, G. Deng, S. Yoo, K. Lee, B.-H. Lee, T. Hyeon and M. S. Bootharaju, *Nanoscale*, 2024, **16**, 12329–12344.
11 O. Fuhr, S. Dehnen and D. Fenske, *Chem. Soc. Rev.*, 2013, **42**, 1871–1906.
12 N. K. Chaki, J. Sharma, A. B. Mandle, I. S. Mulla, R. Pasricha and K. Vijayamohanan, *Phys. Chem. Chem. Phys.*, 2004, **6**, 1304–1309.
13 M. Schmidt, A. Masson, H.-P. Cheng and C. Brechignac, *Chem. Phys. Chem.*, 2015, **16**, 855–865.
14 M. L. McKee and A. Samokhvalov, *J. Phys. Chem. A*, 2017, **121**, 5018–5028.

15 L. Fu, Q. Du, L. Sai and J. Zhao, *J. Phys. Chem. Lett.*, 2024, **15**, 9160–9166.
16 P. Schnabel, W. Wiese and M. P. Irion, *Ber. Bunsenges. Phys. Chem.*, 1990, **1282**, 1278–1282.
17 R. A. Flurer and K. L. Busch, *J. Am. Chem. Soc.*, 1991, **113**, 3656–3663.
18 Y. Chen and P. B. Armentrout, *J. Chem. Phys.*, 1995, **103**, 618–625.
19 C. Bréchignac, P. Cahuzac, J. Leygnier and I. Tignères, *Chem. Phys. Lett.*, 1999, **303**, 304–310.
20 L. D. Socaciu, J. Hagen, U. Heiz, T. M. Bernhardt, T. Leisner and L. Wöste, *Chem. Phys. Lett.*, 2001, **340**, 282–288.
21 M. J. Manard, P. R. Kemper and M. T. Bowers, *Int. J. Mass Spectrom.*, 2003, **228**, 865–877.
22 M. Schmidt, P. Cahuzac, C. Bréchignac and H. P. Cheng, *J. Chem. Phys.*, 2003, **118**, 10956–10962.
23 M. Schmidt, A. Masson and C. Bréchignac, *J. Chem. Phys.*, 2005, **122**, 134712.
24 T. M. Bernhardt, *Int. J. Mass Spectrom.*, 2005, **243**, 1–29.
25 J. Ma, X. Cao, H. Liu, B. Yin and X. Xing, *Phys. Chem. Chem. Phys.*, 2016, **18**, 12819–12827.
26 M. Arakawa, M. Horioka, K. Minamikawa, T. Kawano and A. Terasaki, *J. Phys. Chem. C*, 2020, **124**, 26881–26888.
27 G. N. Khairallah and R. A. J. O'Hair, *Dalton Trans.*, 2008, 2956–2965.
28 H. Nagao, M. Toyoda, S. Hayakawa, K. Iwamoto, T. Ichihara, K. Kawamura and K. Awazu, *Eur. J. Mass Spectrom.*, 2009, **15**, 459–469.
29 S. Bhowmick, A. Maisser, Y. V. Suleimanov, A. Schmidt-Ott and G. Biskos, *J. Phys. Chem. A*, 2022, **126**, 6376–6386.
30 M. Doust Mohammadi, S. Bhowmick, A. Maisser, A. Schmidt-Ott and G. Biskos, *Phys. Chem. Chem. Phys.*, 2024, **26**, 14547–14560.
31 C. R. Landis and F. Weinhold, *Inorg. Chem.*, 2013, **52**, 5154–5166.
32 C. R. Landis and F. Weinhold, *The NBO View of Chemical Bonding*, John Wiley & Sons, Ltd, 2014, pp. 91–120.
33 R. L. DeKock, R. D. Van Zee and T. Ziegler, *Inorg. Chem.*, 1987, **26**, 563–567.
34 V. Bonacic-Koutecky, M. Boiron, J. Pittner, P. Fantucci and J. Koutecký, *Eur. Phys. J. D*, 1999, **9**, 183–187.
35 P. Weis, T. Bierweiler, S. Gilb and M. M. Kappes, *Chem. Phys. Lett.*, 2002, **355**, 355–364.
36 G. N. Khairallah and R. A. J. O'Hair, *Dalton Trans.*, 2005, 2702–2712.
37 S. Zhao, Z.-P. Liu, Z.-H. Li, W.-N. Wang and K.-N. Fan, *J. Phys. Chem. A*, 2006, **110**, 11537–11542.
38 J. Roithová and D. Schröder, *J. Am. Chem. Soc.*, 2007, **129**, 15311–15318.
39 Y. Wang and X. G. Gong, *J. Nanosci. Nanotechnol.*, 2010, **10**, 5500–5506.
40 K. Duanmu and D. G. Truhlar, *J. Phys. Chem. C*, 2015, **119**, 9617–9626.
41 J. Van Der Tol, D. Jia, Y. Li, V. Chernyy, J. M. Bakker, M. T. Nguyen, P. Lievens and E. Janssens, *Phys. Chem. Chem. Phys.*, 2017, **19**, 19360–19368.
42 J. Cížek, *Adv. Chem. Phys.*, 1969, 35–89.
43 R. J. Bartlett, *Annu. Rev. Phys. Chem.*, 1981, **32**, 359–401.
44 G. D. Purvis and R. J. Bartlett, *J. Chem. Phys.*, 1982, **76**, 1910–1918.
45 F. Q. Wang, G. N. Khairallah and R. A. O'Hair, *Int. J. Mass Spectrom.*, 2009, **283**, 17–25.
46 R. Mitric, J. Petersen, A. Kulesza, M. I. S. Röhr, V. Bonacic-Koutecky, C. Brunet, R. Antoine, P. Dugourd, M. Broyer and R. A. J. O'Hair, *J. Phys. Chem. Lett.*, 2011, **2**, 548–552.
47 A. Zavras, G. N. Khairallah, M. Krsti, M. Girod, S. Daly, R. Antoine, P. Maitre, R. J. Mulder, S.-A. Alexander, V. Bonacic-Koutecký, P. Dugourd and R. A. J. O'Hair, *Nat. Commun.*, 2016, **7**, 11746.
48 J. Zhang and V.-A. Glezakou, *Int. J. Quantum Chem.*, 2021, **121**, e26553.
49 E. A. Mason and E. W. McDaniel, *Transport Properties of Ions in Gases*, John Wiley & Sons, Inc., New York, 1988.
50 D. F. Hagen, *Anal. Chem.*, 1979, **51**, 870–874.
51 M. F. Mesleh, J. M. Hunter, A. A. Shvartsburg, G. C. Schatz and M. F. Jarrold, *J. Phys. Chem.*, 1996, **100**, 16082–16086.
52 A. Maisser, K. Barmpounis, M. B. Attoui, G. Biskos and A. Schmidt-Ott, *Aerosol Sci. Technol.*, 2015, **49**, 886–894.
53 A. Maisser, K. Barmpounis, S. Holm, M. Attoui, A. Schmidt-Ott, J. Kangasluoma and G. Biskos, *J. Aerosol Sci.*, 2021, **156**, 105780.
54 A. Laio and M. Parrinello, *Proc. Natl. Acad. Sci. U. S. A.*, 2002, **99**, 12562–12566.
55 J. Yu, N. Q. Su and W. Yang, *JACS Au*, 2022, **2**, 1383–1394.
56 J. S. Murray and P. Politzer, *Comput. Mol. Sci.*, 2011, **1**, 153–163.
57 E. Scrocco and J. Tomasi, *New Concepts II*, Berlin, Heidelberg, 1973, pp. 95–170.
58 R. F. W. Bader, *Atoms in Molecules: A Quantum Theory*, Clarendon Press, Oxford, 1990.
59 P. L. A. Popelier, *The Chemical Bond*, John Wiley & Sons, Ltd, 2014, pp. 271–308.
60 E. R. Johnson, S. Keinan, P. Mori-Sanchez, J. Contreras-Garcia, A. J. Cohen and W. Yang, *J. Am. Chem. Soc.*, 2010, **132**, 6498–6506.
61 J. Zhang and M. Dolg, *Phys. Chem. Chem. Phys.*, 2015, **17**, 24173–24181.
62 J. Zhang and M. Dolg, *Phys. Chem. Chem. Phys.*, 2016, **18**, 3003–3010.
63 J. Zhang, V.-A. Glezakou, R. Rousseau and M.-T. Nguyen, *J. Chem. Theory Comput.*, 2020, **16**, 3947–3958.
64 Y. Zhao and D. G. Truhlar, *Theor. Chem. Acc.*, 2008, **120**, 215–241.
65 R. Krishnan, J. S. Binkley, R. Seeger and J. A. Pople, *J. Chem. Phys.*, 1980, **72**, 650–654.
66 D. Andrae, U. Häußermann, M. Dolg, H. Stoll and H. Preuß, *Theor. Chim. Acta*, 1990, **77**, 123–141.
67 M. Chen, J. E. Dyer, K. Li and D. A. Dixon, *J. Phys. Chem. A*, 2013, **117**, 8298–8313.
68 M. J. Frisch, G. W. Trucks, H. B. Schlegel, G. E. Scuseria, M. A. Robb, J. R. Cheeseman, G. Scalmani, V. Barone, G. A. Petersson, H. Nakatsuji, X. Li, M. Caricato, A. V. Marenich,

J. Bloino, B. G. Janesko, R. Gomperts, B. Mennucci, H. P. Hratchian, J. V. Ortiz, A. F. Izmaylov, J. L. Sonnenberg, D. Williams-Young, F. Ding, F. Lipparini, F. Egidi, J. Goings, B. Peng, A. Petrone, T. Henderson, D. Ranasinghe, V. G. Zakrzewski, J. Gao, N. Rega, G. Zheng, W. Liang, M. Hada, M. Ehara, K. Toyota, R. Fukuda, J. Hasegawa, M. Ishida, T. Nakajima, Y. Honda, O. Kitao, H. Nakai, T. Vreven, K. Throssell, J. A. Montgomery Jr., J. E. Peralta, F. Ogliaro, M. J. Bearpark, J. J. Heyd, E. N. Brothers, K. N. Kudin, V. N. Staroverov, T. A. Keith, R. Kobayashi, J. Normand, K. Raghavachari, A. P. Rendell, J. C. Burant, S. S. Iyengar, J. Tomasi, M. Cossi, J. M. Millam, M. Klene, C. Adamo, R. Cammi, J. W. Ochterski, R. L. Martin, K. Morokuma, O. Farkas, J. B. Foresman and D. J. Fox, *Gaussian 16 Revision C.01*, 2016.

69 T. H. Dunning, *J. Chem. Phys.*, 1989, **90**, 1007–1023.

70 R. A. Kendall, T. H. Dunning and R. J. Harrison, *J. Chem. Phys.*, 1992, **96**, 6796–6806.

71 K. A. Peterson and C. Puzzarini, *Theor. Chem. Acc.*, 2005, **114**, 283–296.

72 R. O. Ramabhadran and K. Raghavachari, *J. Chem. Theory Comp.*, 2013, **9**, 3986–3994.

73 J. C. Rienstra-Kiracofe, W. D. Allen and H. F. Schaefer, *J. Phys. Chem. A*, 2000, **104**, 9823–9840.

74 S. R. Miller, N. E. Schultz, D. G. Truhlar and D. G. Leopold, *J. Chem. Phys.*, 2009, **130**, 024304.

75 H.-J. Werner, P. J. Knowles, *et al.*, MOLPRO, Version 2022.3, A Package of Ab Initio Programs, 2024.

76 H.-J. Werner, P. J. Knowles, G. Knizia, F. R. Manby and M. Schütz, *WIREs Comput. Mol. Sci.*, 2012, **2**, 242–253.

77 J.-D. Chai and M. Head-Gordon, *Phys. Chem. Chem. Phys.*, 2008, **10**, 6615–6620.

78 J. Harle and M. Cafiero, *J. Phys. Chem. B*, 2025, **129**, 4879–4894.

79 G. J. Martyna, M. L. Klein and M. Tuckerman, *J. Chem. Phys.*, 1992, **97**, 2635–2643.

80 G. Bussi, D. Donadio and M. Parrinello, *J. Chem. Phys.*, 2007, **126**, 014101.

81 F. Neese, *WIRES Comput. Mol. Sci.*, 2022, **12**, e1606.

82 L. S. Sremaniak, L. Perera and M. L. Berkowitz, *J. Phys. Chem.*, 1996, **100**, 1350–1356.

83 C. Larriba and C. J. Hogan, *J. Comput. Phys.*, 2013, **251**, 344–363.

84 V. Shrivastav, M. Nahin, C. J. Hogan and C. Larriba-Andaluz, *J. Am. Soc. Mass Spectrom.*, 2017, **28**, 1540–1551.

85 I. Campuzano, M. F. Bush, C. V. Robinson, C. Beaumont, K. Richardson, H. Kim and H. I. Kim, *Anal. Chem.*, 2012, **84**, 1026–1033.

86 P. Weis, O. Welz, E. Vollmer and M. M. Kappes, *J. Chem. Phys.*, 2004, **120**, 677–684.

87 T. Koopmans, *Physica*, 1934, **1**, 104–113.

88 R. G. Parr and R. G. Pearson, *J. Am. Chem. Soc.*, 1983, **105**, 7512–7516.

89 R. G. Parr, L. V. Szentpaly and S. Liu, *J. Am. Chem. Soc.*, 1999, **121**, 1922–1924.

90 R. G. Parr and Z. Zhou, *Acc. Chem. Res.*, 1993, **26**, 256–258.

91 E. D. Glendening, C. R. Landis and F. Weinhold, *J. Am. Chem. Soc.*, 2019, **141**, 4156–4166.

92 A. E. Reed, R. B. Weinstock and F. Weinhold, *J. Chem. Phys.*, 1985, **83**, 735–746.

93 E. D. Glendening, J. K. Badenhoop, A. E. Ree, J. E. Carpenter, J. A. Bohmann, C. M. Morales, P. Karafiloglou, C. R. Landis and F. Weinhold, *NBO 7.0*, 2018.

94 R. F. W. Bader, S. G. Anderson and A. J. Duke, *J. Am. Chem. Soc.*, 1979, **101**, 1389–1395.

95 S. R. Gadre, C. H. Suresh and N. Mohan, *Molecules*, 2021, **26**, 3289.

96 P. S. V. Kumar, V. Raghavendra and V. Subramanian, *J. Chem. Sci.*, 2016, **128**, 1527–1536.

97 A. D. Becke and K. E. Edgecombe, *J. Chem. Phys.*, 1990, **92**, 5397–5403.

98 K. Koumpouras and J. A. Larsson, *J. Phys.: Condens. Matter*, 2020, **32**, 315502.

99 H. Jacobsen, *Can. J. Chem.*, 2008, **86**, 695–702.

100 T. Lu and F. Chen, *J. Comput. Chem.*, 2012, **33**, 580–592.

101 F. Schmidt-Ott, S. Bhowmick, A. Lekkas, D. Papanastasiou, A. Maisser and G. Biskos, *Atmos. Meas. Tech.*, 2025, **18**, 7075–7083.

102 R. Guardiola and J. Navarro, *J. Phys. Chem. A*, 2011, **115**, 6843–6850.

103 P. Marcos, J. Alonso, A. Rubio and M. López, *Eur. Phys. J. D*, 1999, **6**, 221–233.

104 C. P. Singh, P. P. Samal and S. Krishnamurty, *Theor. Chem. Acc.*, 2021, **140**, 132.

105 Z. Xu, J. Gao, Z. Xu, M. Attoui, X. Pei, M. Amo-González, K. Zhang and Z. Wang, *Atmos. Meas. Tech.*, 2023, **16**, 5995–6006.

106 R. S. Glaskin, M. A. Ewing and D. E. Clemmer, *Anal. Chem.*, 2013, **85**, 7003–7008.

107 C. N. Naylor and G. Nagy, *Mass Spectrom. Rev.*, 2025, **44**, 581–598.

108 L. G. M. Pettersson, J. Bauschlicher, W. Charles, S. R. Langhoff and H. Partridge, *J. Chem. Phys.*, 1987, **87**, 481–492.

109 Y. Cai, X. Sun and X. Huang, *Comput. Theor. Chem.*, 2018, **1134**, 15–21.

110 I. R. Ariyarathna, *Molecules*, 2025, **30**, 2435.

111 N. S. Phala, G. Klatt and E. van Steen, *Chem. Phys. Lett.*, 2004, **395**, 33–37.

112 L. Lundberg, P. Martini, M. Goulart, M. Gatchell, D. K. Bohme and P. Scheier, *J. Am. Soc. Mass Spectrom.*, 2019, **30**, 1906–1913.

113 X.-J. Kuang, X.-Q. Wang and G.-B. Liu, *J. Chem. Sci.*, 2011, **123**, 743–775.

114 M. Takenouchi, S. Kudoh, K. Miyajima and F. Mafuné, *J. Phys. Chem. A*, 2015, **119**, 6766–6772.